CO_2-Brine flow in Nubian Sandstone (Egypt): Pore Network Modeling using Computerized Tomography Imaging

Mahmoud Hefny[1,5], ChaoZhong Qin[2], Anozie Ebigbo[1], Jeff Gostick[3], Martin O. Saar[1], Mohamed Hammed[4]

[1] Geothermal Energy and Geofluids, Institute of Geophysics, ETH Zürich, Switzerland

[2] Mechanical Engineering Department, Technology University of Eindhoven, The Netherlands

[3] Department of Chemical Engineering, University of Waterloo, Canada

[4] Geology Department, Cairo University, Egypt

[5] Geology Department, South Valley University, Egypt

mhefny@ethz.ch

Keywords: Pore-Network Modeling, CO_2-Plume Geothermal, Nubian sandstone, residual trapping.

ABSTRACT

The injection of CO_2 into the highly permeable Nubian Sandstone of a depleted oil field in the central Gulf of Suez Basin **(**Egypt**)** is an effective way to extract enthalpy from deep sedimentary basins while sequestering CO_2, forming a so-called CO_2-Plume Geothermal (CPG) system. Subsurface flow models require constitutive relationships, including relative permeability and capillary pressure curves, to determine the CO_2-plume migration at a representative geological scale.

Based on the fluid-displacement mechanisms, quasi-static pore-network modeling has been used to simulate the equilibrium positions of fluid-fluid interfaces, and thus determine the capillary pressure and relative permeability curves. 3D images with a voxel size of 650 nm^3 of a Nubian Sandstone rock sample have been obtained using Synchrotron Radiation X-ray Tomographic Microscopy. From the images, topological properties of pores/throats were constructed. Using a pore-network model, we performed a cycle of primary drainage of quasi-static invasion to quantify the saturation of $scCO_2$ at the point of a breakthrough with emphasis on the relative permeability–saturation relationship.

We compare the quasi-static flow simulation results from the pore-network model with experimental observations. It shows that the P_c-S_w curve is very similar to those observed experimentally.

1. INTRODUCTION

The continuous rise in atmospheric CO_2 concentrations due to the combustion of fossil fuels could, if not abated, lead to irreversible consequences (Hartfield et al., 2018). Carbon Capture and Storage (CCS) is a process whereby CO_2 is captured from flue gases and injected in supercritical or liquefied form into suitable subsurface formations. However, it is possible to combine CCS with geothermal energy by using CO_2 as the geothermal working fluid. This so-called CO_2-Plume Geothermal (CPG) system has been suggested for permeable geological formations (e.g. Adams, Kuehn, Bielicki, Randolph, & Saar, 2014, 2015; Garapati, Randolph, & Saar, 2015; Randolph & Saar, 2011). Numerous oil/gas reservoirs in the Gulf of Suez (Egypt), that are either in the depletion phase or already depleted, may be suitable for CPG development. During CPG, the subsurface CO_2 plume absorbs heat from the host rock and migrates from injection to production boreholes, displacing the native formation fluid (e.g., brine).

Because of the difficulties inherent in the prediction of CO_2-brine flow in deep reservoirs, analyzing capillary interactions at the pore scale in order to obtain the constitutive relationship between capillary pressure (P_c), or relative permeability, and saturation (S) is required. Such multiphase fluid flow is controlled by a variety of interdependent physical factors; including the actual topology of the porous medium and the fluid properties, for example, viscosity, contact angle, and surface tension (Andrew, Menke, Blunt, & Bijeljic, 2015).

Pore-scale numerical modeling of immiscible multi-phase flow in a complex porous medium is often employed to obtain the macroscopic continuum properties of geological media such as capillary pressure, relative permeability curves and pore-scale displacement mechanisms (e.g. Berg et al., 2016; Blunt et al., 2013; Patzek, 2001 and references therein). Pore-scale models can be broadly divided into pore-network models, lattice-gas models, lattice-Boltzmann models, and molecular dynamics models. The key to the success of a pore-network model (PNM) is to extract pore network information that strictly preserves the pore connectivity expressed in the pore space images and assign to each (network) element a set of geometric properties (e.g. size and shape) that closely match the values measured directly from the images.

High-resolution Synchrotron Radiation X-ray Tomographic Microscopy (SRXTM) is a powerful tool for non-destructive and quantitative investigations of the internal topology of microstructures. The application of high-flux synchrotron radiation in the

hard X-ray range gives improved time and spatial resolution, permitting the visualization of features down to the sub-micrometer levels.

The constant improvement in both computational power and imaging capacity allows usage of the discretized images as a computational mesh to perform quasi-static and dynamic fluid invasion simulations directly inside the pore structure (Dong & Blunt, 2009; Gostick, 2017). These results can complement laboratory experiments for understanding fluid-displacement mechanisms in a representative elementary volume (REV).

The main purpose of this paper is to develop a model to describe and quantify the fluid-displacement mechanisms in a geologically realistic pore network. Using High-Performance Computing (HPC), the essential geometrical and topological properties of Nubian sandstone rock samples, obtained from the Gulf of Suez (Egypt), have been extracted. This includes the following steps: (1) identification of the boundary of the solid phase and the void phase, (2) recognition of the pore bodies and the smallest crevices (throat connecting at least two pore bodies), and (3) description of the geometry of the pore-network elements with a shape factor to investigate various displacement mechanisms being simulated.

In this paper, we provide a numerical approach for a primary drainage simulation in a fully water-saturated natural porous medium (i.e. invasion of non-wetting phase into a saturated pore network with a wetting phase) to get capillary pressure-saturation and relative permeability-saturation curves, at the pore scale. We use synchrotron radiation X-ray microtomographic microscopy data to predict multiphase transport properties. The simulation results are benchmarked against rigorous experimental data obtained from the Rock Deformation Laboratory and the Clay Laboratory at ETH Zürich.

2. IMAGE ANALYSIS

2.1 Sample Characterization

The Nubian Sandstone, East-central Gulf of Suez (cGOS), Egypt, where geothermal anomalies exist, is acts as a convection cell for hot geothermal fluids (Hollis et al., 2017). The apparently high geothermal potential of the region may be attributed to the conjunction between the present-day surface thermal manifestations and the locations of Oligo-Miocene volcanic activity along major rift-related faults (Hefny et al., in preparation). Oriented rock blocks of Nubian Sandstone, therefore, have been retrieved from cGOS for further geothermics-related investigations.

Optical microscopy analysis was complemented by automated QEMSCAN® (Quantitative Evaluation of Minerals by Scanning Electron Microscopy) Quanta 650F technique at the University of Geneva, providing quantitative mineralogical compositions at a scanning resolution of 5 µm. Here, the mineral identification maps were based on back-scattered electron values, energy-dispersive X-ray spectra, and X-ray count rates. All these tools were integrated to assess the mineralogical composition and rock type.

The QEMSCAN shows that the majority of distinguished mineral phases in the Nubian Sandstone are medium to fine quartz grains (85%) with few kaolinites as clay mineral (8%), 5% k-feldspar, and 2% other minerals trapped within the pore-system; Figure 1. The quartz grain types, which, in turn, are mainly monocrystalline with rare strained polycrystalline, are cemented by silica. This Palaeozoic quartz arenite sandstone deposited in continental to fluvial braided systems. It represents the primary prolific conventional reservoir in GOS. Having such a quartz-dominated system, neither mineral dissolution/precipitation nor clay swelling will be significant during the quasi-static simulation.

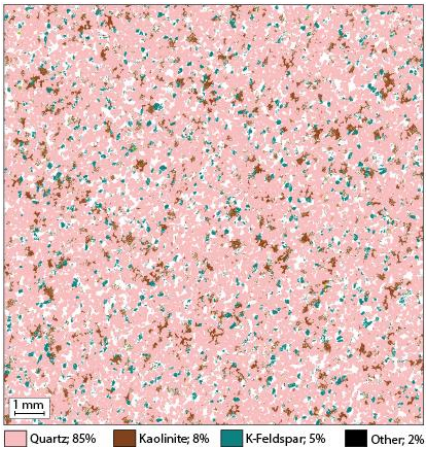

Figure 1: QEMSCAN image of arkose fine-grained Nubian sandstone.

For the laboratory rock physics experiments, three mutual cylindrical plugs of 25.5 mm in diameter and >30 mm in height were cored from the oriented rock block to investigate the intrinsic rock properties and anisotropy influence on fluid-flow. A lathe machine has been used to produce the highest quality of parallelism for the upper and lower surface of the cylindrical plugs, with ±5 µm precision. The plugs were dried in an oven at 100°C for at least 48 hours to remove trapped fluid in pores. Before performing any further measurements, the plugs were stored in a desiccator with silica gel to prevent moisture from re-entering plugs.

Using a gas-displacement-based apparatus (He-pycnometer Accupyc II 1340, micromeritics), the matrix volumes of the cylindrical plugs have been determined at ambient conditions in a range that keeps the standard deviation of every single measurement at a value lower than 5%. Beforehand, the plugs' masses were measured using a highly precise balance ($\pm 5.0\times10^{-7}$ kg tolerance). Using the predefined parameters, including the bulk volume, matrix volume, and dry mass, the grain density and the effective porosity (i.e. the volume of interconnected pores) have been calculated. The anisotropy value (porosity here) is

<5%, we, therefore, consider here the isotropic nature of Nubian Sandstone.

The same scanned subplug was used to perform High-pressure system Mercury Intrusion Porosimetry (MIP) to evaluate the pore radius, pore size volume/distribution, and porosity-related characteristics of Nubian sandstone based on the behavior of non-wetting liquids in a capillary following the Young-Laplace relationship. The experiment was having formed initially under a low pressure (40 MPa), followed by high pressures of up to 400 MPa. At 400 MPa, mercury can be forced to invade pores as small as 5 nm in radius, constituting microporosity (Kärger, 2011). Nevertheless, under high capillary pressures, the wetting phase (air) is pushed farther into the corners, as the radius of curvature of the interface decreases. To validate the results from our PN quasi-static simulator, we compare the pore volume density data and the scaled air-mercury P_c-S_w experimental curve with the simulation results extracted from the 3D rock model. Mercury Intrusion Porosimetry (MIP) shows a lognormal pore-size distribution in our Nubian Sandstone samples. Moreover, it shows that the majority of the pore bodies fall within the resolvable range of our imaging capacity (Figure 2).

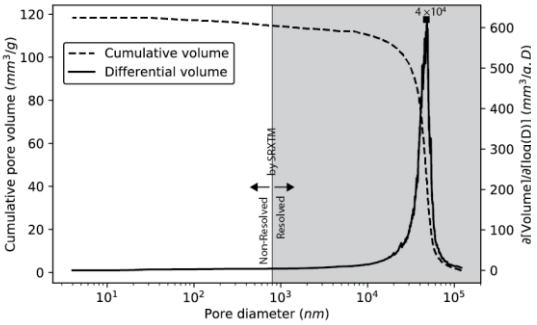

Figure 2: Pore-size distribution of the Nubian Sandstone sample, and cumulative mercury volume intruded as a function of pore-throat radius and pressure. Both are determined by Mercury Intrusion Porosimetry (MIP). The grey area represents the zone resolved by SRXTM, where the pores in the Nubian Sandstone are located.

2.2 Imaging

High-resolution Synchrotron Radiation X-ray Tomographic Microscopy (SRXTM) is a powerful tool for non-destructive and quantitative investigations of the internal topology of microstructures. The SRXTM measurements were conducted on a cylindrical subplug [with 6 mm diameter and ~10 mm length that was recovered from the main plug] in a static medium, that is one with a morphology that does not change during deformation/thermochemical processes. The parallelism of the ends of the cylindrically shaped subplug was achieved by gently grinding the cuttings, first on the side on a rock saw blade, then by hand using sandpaper (grit 120).

The imaging workflow was performed at the TOmorgraphic Microscopy and Coherent rAdiology experimenTs (TOMCAT) beamline station with third-generation synchrotron facilities at the Swiss Light Source, Paul Scherrer Institute, Switzerland (see Marone & Stampanoni, 2012 for technical specifications). For the best-contrast phases (pore and solid), the sample was exposed to a parallel beam of monochromatic synchrotron X-ray radiation for 500 ms exposure time at 26 keV photon energy and 401.25 mA ring current. This beam energy is optimized to provide sufficient photon flux, capable of penetrating the 6 mm diameter subplug and ensuring the best image contrast (signal-to-noise ratio). The lower-energy X-rays that hit the cylindrical subplug and do not improve imaging were filtered out using 100µm Al, 10µm Cu, and 10µm Fe sheets, while the remaining X-rays hit the cylindrical subplug. The field of view (FOV) covered 1.3×1.4 mm^2 of the original size of the subplug.

The transmitted X-rays were converted into visible light by a cerium-doped lutetium aluminum garnet (LuAG: 20 µm) scintillator and projected at 10× magnification onto a high-speed CMOS camera (PCO.Edge 5.5; PCO AG, Germany) with 2560×2160 pixels, leading to an effective pixel width of 0.65µm. A sample-to-scintillator distance of 36 mm yielded a small amount of edge enhancement in the images.

Each tomogram was computed from 1,801 projections (500 ms exposure time) over a 180° rotation by a gridded Fourier transform-based reconstruction algorithm with a Parzen filter using a filtered backprojection algorithm (Marone & Stampanoni, 2012). Projections were magnified by microscope optics and digitized by a high-resolution CCD camera, which results in 8-bit (256 grey values) tif-format gray images.

The reconstruction center was found for the first and last image in the sequence and linearly interpolated between these two values for the others. The reconstructed volumes were filtered with a 3×3×3 median filter, segmented with local connectivity-based thresholding, and processed furthered as described in the next section. The image datasets were then cropped around the core so each one consisted of around 2160×2160×2160 (~10.0×10^9 grid cells) pixels with a voxel size of 650 nm^3 at 10-fold optical magnification.

2.3 Image processing and segmentation

The gray-level SRXTM images of the Nubian Sandstone have only one identifiable mineral phase (Quartz) with sharp edges (Figure 3A). The attenuation coefficient of the X-ray (grayscale intensities) in the mineral phase is higher than the attenuation coefficient in pore spaces (darker gray). A bimodal histogram for each image, therefore, was applied using Otsu's method of automatically thresholding the images (Otsu, 1979); Figure 3B. The threshold value was set for the local minimum to alleviate spurious creation of catchment basins.

Image segmentation is done by delineating and labeling sets of pixels within the domain of gray-level SRXTM images into a number of disjoint nonempty sets of objects/phases/segments depending on the gray-level histogram, neighborhood information, and the prior knowledge of the statistic in the images (Soille, 2014). The watershed transformation, which treats pixel values as local topography, was used to segment the images. However, watershed segmentation does not straightforwardly provide acceptable results due to the over-segmentation. Alleviating this effect will now be elaborated upon in what follows.

After thresholding, a labeling procedure was performed on the obtained binary images to isolate and quantify each individual object/phase using the Euclidian distance map. Distance transform of a bi-level image is defined by the shortest distance from every pixel to the nearest non-zero foreground-valued pixel and is employed to distinguish between the pores and the throats (Figure 3D). A Gaussian blur filter was applied on the distance transform map to smooth it and to minimize spurious peaks created due to the flat nature of the solids voxelated in the images.

Removal of the erroneous peaks that lead to over-segmentation was done individually and in an iterative way using a minimal cubic structuring element during morphology dilation. The similarity between the maximized dilated peaks and the smooth distance map allows the recognition of new peak(s). The comparison between the old peak(s) and new peak(s) allows elimination of the spurious errors. This is followed by applying the marker-based watershed transformation at the local minima of a hypothetical 3D topography, from which basins are flooded to segment the images (Figure 3E). A detailed description of the extraction algorithm is given in Gostick (2017). Table 1 and Figure 4 provide the results of the extracted pore/pore-throat network for pore-scale modeling/simulation as well as laboratory experiments validation.

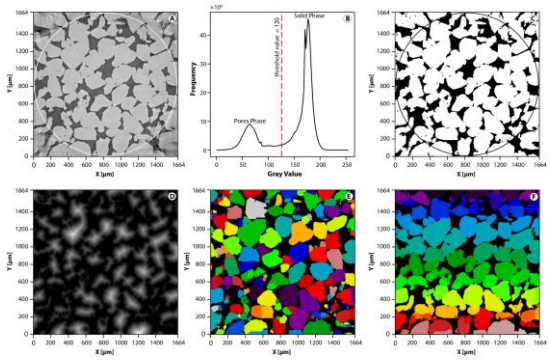

Figure 3: Illustration of marker-based watershed segmentation. [A] Two-dimensional cross-section of a Nubian Sandstone grey image. [B] Histogram grayscale intensity shows well separated peaks for the void spaces and the solid voxels in a bimodal distribution profile. [C] Binarization of the gray image. [D] Distance transform map. [E] The segmentation results of pore regions. [F] Pore body and throat connectivity.

2.4 Pore Network Construction

Construction of the stochastic pore network, including the pore- and throat-size distributions as well as their connectivities, was performed using the open-source PoreSpy package, while the OpenPNM package was dedicated to data storage and handling (Gostick, 2017; Gostick et al., 2016). A summary of the extracted pore network is presented in Figure 4, where the pores appear to be properly located. The distributions of inscribed radii are shown in Figure 5, and Table 1 provides the statistical information of the pore network.

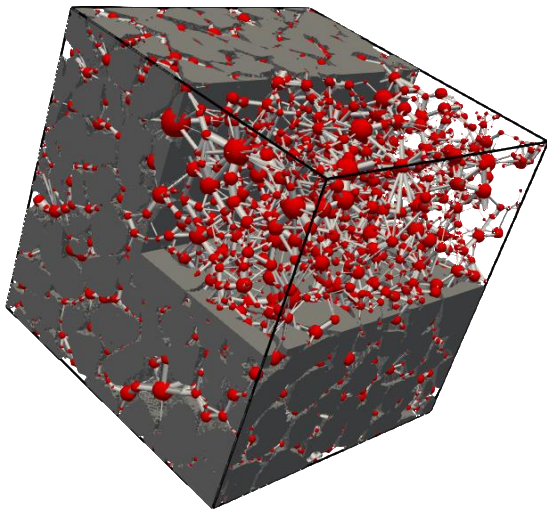

Figure 4: 3D view of the Nubian Sandstone sample (2160×2160×2160). The voxel image shows the solid phase in grey while the extracted pore elements are overlain. The pores are represented by the red spheres that are smaller than their actual sizes to improve the visualization.

Table 1: Parameter statistics of the pore network of the Nubian Sandstone sample, extracted by the stochastic pore-network extractor.

Pore-Network Parameter	Value	Unit
Network size (domain)	1.41×1.41×1.41	[mm^3]
Total number of pores	4334	
Pores extended diameter; d_{pe}	$8.1 < d_{pi} < 192.28$: Average: 49.73 (*)	[µm]
Pores inscribed diameter; d_{pi}	$5.18 < d_{pe} < 115.6$; Average: 28.71 (*)	[µm]
Total number of throats	8939	
Throats extended diameter; d_{tp}	$2.59 < d_{ti} < 129.47$: Average: 26.83	[µm]
Throats inscribed diameter; d_{ti}	$4.38 < d_{tp} < 91.03$: Average: 20.83 (*)	[µm]

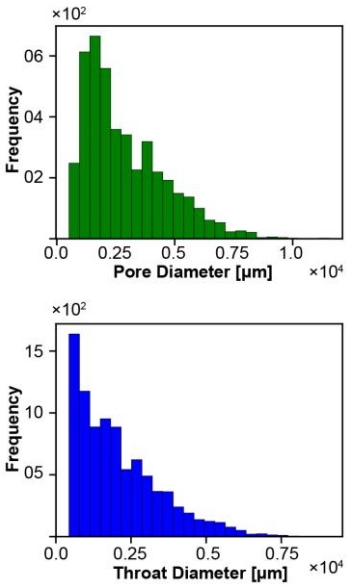

Figure 5: Diameter of pore boday and throat of the extracted PNM for Nubian Sandstone.

2.5 Representative Elementary Volume

Before simulating two-phase fluid flow within the constructed pore network, the existence of a Representative Elementary Volume (REV) has been confirmed by the spatial distribution of its components to satisfy both a lower and an upper bound of the fluid-flow field. These bounds are required to ensure that the REV is smaller than the flow domain and sufficiently larger than a single pore void or the solid matrix, such that the phase saturations are independent of the REV size and representative of the macroscopic domain. Figure 6A shows that the physical properties (here the porosity) are highly fluctuating as the sub-element volume is small, while they value stabilize and approach the experimental values, measured via different techniques and different sizes, as the volume increases.

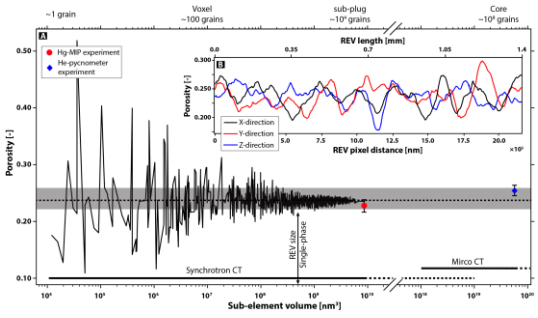

Figure 6: Quantification of the porosity of the Nubian Sandstone sample from SRXTM images. [A] The porosity is calculated for an increasingly large cuboid, starting from a voxel centered in the pore space. Symbols are experimental results of the whole-core sample. The measured MIP skeleton porosity is 26.29%, yielding 3.17% Hg-inaccessible porosity. The grey bar represents the spatial variability zone of porosity. [B] Porosity profile in x-, y-, and z-directions for the REV size of the Nubian Sandstone sample.

The REV size depends on the intrinsic property of the studied material and on the acceptable accuracy to estimate it, as well as on the number of independent realizations that can be measured. The REV of the Nubian Sandstone sample was ~10^9 nm (Figure 6A). The magnitude of porosity anisotropy seems to be negligible at the REV size (Figure 6B). We, therefore, consider here that the Nubian Sandstone sample is isotropic in nature and that local flow always points in the opposite direction of the fluid pressure gradient during the simulation. The anisotropy parameter is essential for the understanding of flow properties in different directions and is a fundamental input parameter for modeling and upscaling pore-network data to the field scale.

2.6 Shape Factor

Mason and Morrow (1991) introduced the shape factor (G) concept to describe the geometry of the pore-network elements (pore body and pore throat) and their angularity for reliable two-phase flow simulations,

$$G=\frac{A}{P^2}, \qquad (1)$$

where A represents the cross-sectional area of a pore or throat and P is its perimeter. Marker-based watershed segmentation provided (i) the region volume (V_{CT}) by summing the number of the voxels in that region [black voxels in Figure 3D], (ii) the extended radius (R_{CT}^{ext}), given as half of the maximum value of the global distance map, lying within each pore region, that can be extend to the neighbouring pores, and (iii) the inscribed radius (R_{CT}^{ins}), given as half of the maximum value of the local distance map, lying within each pore region. The idealized pore length (L_{PNM}) is equal to summing the extended radius and the inscribed radius.

The cross-sectional area of an idealized pore body (A_{PNM}) and its perimeter (P_{PNM}), therefore, can be defined by Equations [2] and [3], respectively,

$$A_{PNM}=\frac{V_{CT}}{R_{CT}^{ins}+R_{CT}^{ext}}, \qquad (2)$$

$$P_{PNM}=\frac{2V_{CT}}{R_{CT}^{ins}(R_{CT}^{ins}+R_{CT}^{ext})}, \qquad (3)$$

For pore throats, marker-based watershed segmentation counts the number of voxels in the throat with a distance transform value of 1, then multiplies the result by the voxel length to provide the throat's perimeter. Its inscribed radius can be found from the maxima of the global distance transform.

The shape factor has the same cross section as the real system from which the pore network is derived. From Equation [1], the shape factor values of √3/36, 1/4π, 1/16 correspond to, respectively, the 2D cross section of a scalene triangle, square, and circle.

3. NUMERICAL METHODS

Over the last few decades, several studies have estimated fluid-flow properties from digital images of

rocks (e.g. Blunt et al., 2013; Krevor et al., 2015; K. Rasmusson, Rasmusson, Tsang, & Niemi, 2016; M. Rasmusson, 2018; Valvatne & Blunt, 2004). In this paper, incompressible and immiscible two-phase laminar flow in a natural porous medium (Nubian Sandstone) is considered, where one fluid, supercritical CO_2 ($scCO_2$), is the non-wetting phase, while the other (Brine with a salinity of ~40 ppt) is the wetting-phase. The salinity value refers to the water salinity of the Gulf of Suez after Gavish (1974). We assume that such brine is fully filling the pore network of the Nubian Sandstone. A quasi-static PNM simulator for $scCO_2$ invasion (drainage) after Qin et al., (2016) has been modified for this study yielding capillary pressure and relative permeability curves.

- The capillary pressure curve is achieved by simulating an invasion-percolation process, while
- Two-phase relative permeabilities are calculated at each saturation state of the two-phase quasi-static displacements once the system equilibrium is reached.

3.1 Quasi-static modeling of the primary drainage

The pore network, initially fully filled with the wetting phase, is brought in contact with the nonwetting and wetting reservoirs at the inlet and outlet, respectively. Both reservoir pressure values are set to zero. The other boundarie sides are set to no-slip fluid flow. When the primary drainage starts, we continue to increase the nonwetting reservoir pressure by small increments (e.g., 10 Pa). After each increase, we check which pore bodies are invaded by the nonwetting phase. A pore body will be invaded by the nonwetting phase once the following two conditions are both satisfied: (1) the nonwetting reservoir pressure is larger than its entry pressure, (2) both nonwetting and wetting phases in the pore body have pathways to the inlet and outlet reservoirs, respectively. Then, the phase occupation in both pore bodies and pore throats is updated under the equilibrium condition. The used relationships of capillary pressure, with respect to the wetting saturation, are given in Appendix A. The drainage process is terminated once a pre-set maximum drainage pressure is achieved. Finally, the irreducible wetting phase is present in the tight small pores and crevices of the network, due to pore-structure trapping, and resides in the corners of the surface roughness of the pores.

3.2 Calculation of relative permeability

For a given stage in the drainage process, the conducting pathways of the nonwetting and wetting phases are known. For either phase, its volumetric conservation in a pore body is given as:

$$\sum_{j=1}^{N_i} K_{ij}^{\alpha}\left(p_i^{\alpha}-p_j^{\alpha}\right)=0\,, \qquad (4)$$

where i are the pore body index, ij is the pore throat index, N_i is the coordinate number, α is the phase indicator, P [Pa] is the pressure, and K_{ij}^{α} [m^3/Pa/s] is the conductivity calculated by:

$$K_{ij}^{\alpha}=1\Big/\left(\frac{l_i}{2g_i^{\alpha}}+\frac{l_j}{2g_j^{\alpha}}+\frac{l_{ij}}{g_{ij}^{\alpha}}\right), \qquad (5)$$

where l [m] is the length, and g [m^4/Pa/s] is the conductance, given in Appendix A.

With proper inlet and outlet pressure boundary conditions, Equation 4 is solved for the pressure field. Then, Darcy's law is used to obtain the relative permeability for the given network saturation value.

4. RESULTS AND DISCUSSION

The result of the quasi-static single-phase flow simulation shows that the absolute permeability closely converges to the value obtained from the MIP experiment. Table 2 summarizes the intrinsic properties of the Nubian Sandstone sample, using experimental and computational methods. The quasi-static two-phase flow simulation of $scCO_2$-brine shows that the displacement mechanisms during the primary drainage (i.e. at a representative receding contact angle: 50.8°) is a piston-type (*pt*) displacement.

Table 2: Average values of porosity and permeability determined using laboratory experiments and Pore Network (PNM) simulations.

Effective porosity, $\varphi_{effective}$ [%]		Effective permeability, k_{eff} [m^2]	
Laboratory	**SRXTM**	**Laboratory**	**PNM**
26.89 ±0.61*	23.65†	1.70×10^{-12}‡	2.00×10^{-12}"

* Measured via He pycnometry on a larger plug of the same rock (25.4 mm diameter cylindrical sample). This value is based on averaging three plugs with mutual different.

† Calculated from a cylindrical subplug (1.3×1.4 mm), using Synchrotron-based X-ray Computed Tomography

‡ The permeability was determined based on (Kuijpers, Huinink, Tomozeiu, Erich, & Adan, 2017; Equation 08) and using the MIP-processed data including porosity, pore diameter and tortuosity factor.

In the following section, we simulate the non-wetting phase ($scCO_2$ in this case) injection into the wetting-saturated (brine) network. This process is equivalent to the primary drainage process. A visualization of the primary drainage for 10% of irreducible non-wetting saturation is shown in Figure 7. A comparison between the experimental P_c-S_w curve, measured from the MIP experiment (converted from mercury-air to $scCO_2$-brine), and the simulated curve (using our quasi-static pore-network approach) is displayed in Figure 8A. There is a good match between the simulated and the MIP data for the wetting-phase saturation. These curves are drainage capillary pressure curves, since they represent a process during which brine saturation is reduced by increasing the P_c value.

Where $scCO_2$ and brine fluids both reside in the pore network, the ability of each fluid to flow depends on the relative saturation of each phase. This dependency is expressed as a relative permeability-saturation relationship. Figure 8B shows relative permeabilities as a function of wetting saturation for a $scCO_2$-brine system in a natural sandstone.

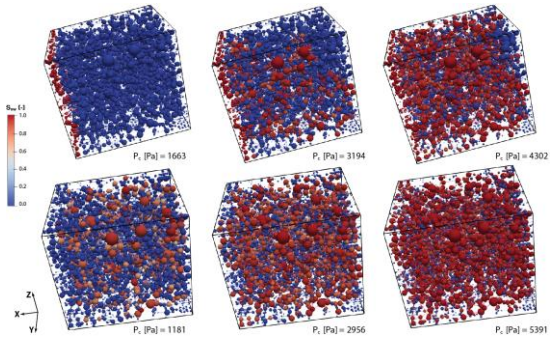

Figure 7: Snapshot of quasi-static simulations with 0.1 irreducible saturation. The upper panel shows representative processes of primary drainage at three different entry pressures, while the lower panel shows imbibition.

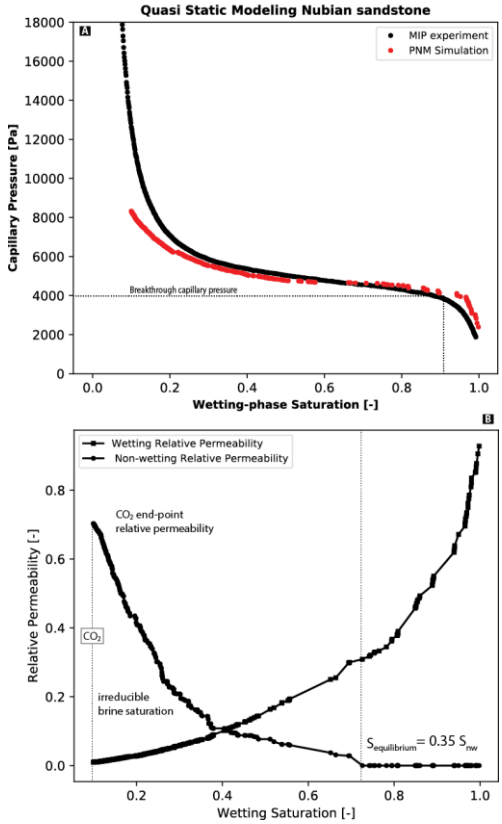

Figure 8: [A] Comparison between a capillary pressure-wetting saturation curve, obtained from PNM simulations, and values measured during primary drainage MIP experiments. [B] Primary drainage relative permeability (k_r–S_w) curves for the $scCO_2$-brine system in the Nubian Sandstone sample, employing PNM simulations.

According to Figure 8B, the non-wetting phase ($scCO_2$) begins to flow at relatively low saturations of the non-wetting phase (i.e. at an equilibrium $scCO_2$ saturation of $S_{equilibrium} \sim 0.35$). The capillary pressure forces the wetting phase (brine in our case) to primarily concentrate in the angularity of small pores at the lowest possible wetting saturation —the residual brine saturation, where the end-point relative permeability for the $scCO_2$ curve is reached (~0.7).

5. CONCLUSIONS AND FUTURE WORK

We have developed a pore-network, quasi-static numerical simulator to study at the pore scale different fluid-displacement mechanisms and investigate (1) the capillary pressure and fluid saturation relationship as well as (2) relative permeabilities as a function of fluid saturation, where viscous forces are negligible, compared to capillarity forces. We have validated the pore-network method by comparing quasi-static flow simulation results with experimental observations for Nubian Sandstone. Our results show that the simulated P_c-S_w curve is similar to those observed experimentally. We conclude that the presented pore-network simulator for natural porous media is sufficiently accurate, efficient and robust to predict pore-scale fluid flow properties.

The constitutive relationships for the porous medium, including the capillary pressure and the relative permeability curves, obtained through our quasi-static modelling approach, will be employed next to estimate the extent of CO_2-plume migration at a representative geological scale. Being the main oil province in Egypt, where depleted oil fields provide subsurface field-scale datasets and proximity to other, albeit intermitted, renewable energy resources and CO_2-emitters, the Gulf of Suez (Egypt) is an urban geologic setting, affording a unique opportunity to develop a hybrid energy system. Such a hybrid system synergistically integrates the CO_2-Plume Geothermal (CPG) system with wind farms and solar parks to provide a reliable and grid-scale electricity supply.

REFERENCES

Adams, B. M., Kuehn, T. H., Bielicki, J. M., Randolph, J. B., & Saar, M. O. (2014). On the importance of the thermosiphon effect in CPG (CO2 plume geothermal) power systems. *Energy*, *69*, 409–418. https://doi.org/10.1016/J.ENERGY.2014.03.032

Adams, B. M., Kuehn, T. H., Bielicki, J. M., Randolph, J. B., & Saar, M. O. (2015). A comparison of electric power output of CO2 Plume Geothermal (CPG) and brine geothermal systems for varying reservoir conditions. *Applied Energy*, *140*, 365–377. https://doi.org/10.1016/J.APENERGY.2014.11.043

Andrew, M., Menke, H., Blunt, M. J., & Bijeljic, B. (2015). The Imaging of Dynamic Multiphase Fluid Flow Using Synchrotron-Based X-ray Microtomography at Reservoir Conditions.

Transport in Porous Media, *110*(1), 1–24. https://doi.org/10.1007/s11242-015-0553-2

Berg, S., Rücker, M., Ott, H., Georgiadis, A., van der Linde, H., Enzmann, F., … Wiegmann, A. (2016). Connected pathway relative permeability from pore-scale imaging of imbibition. *Advances in Water Resources*, *90*, 24–35. https://doi.org/10.1016/J.ADVWATRES.2016.01.010

Blunt, M. J., Bijeljic, B., Dong, H., Gharbi, O., Iglauer, S., Mostaghimi, P., … Pentland, C. (2013). Pore-scale imaging and modelling. *Advances in Water Resources*, *51*, 197–216. https://doi.org/10.1016/J.ADVWATRES.2012.03.003

Dong, H., & Blunt, M. J. (2009). Pore-network extraction from micro-computerized-tomography images. *Physical Review E*, *80*(3), 036307. https://doi.org/10.1103/PhysRevE.80.036307

Garapati, N., Randolph, J. B., & Saar, M. O. (2015). Brine displacement by CO2, energy extraction rates, and lifespan of a CO2-limited CO2-Plume Geothermal (CPG) system with a horizontal production well. *Geothermics*, *55*, 182–194. https://doi.org/10.1016/J.GEOTHERMICS.2015.02.005

Gavish, E. (1974). Geochemistry and mineralogy of a recent sabkha along the coast of Sinai, Gulf of Suez. *Sedimentology*, *21*(3), 397–414. https://doi.org/10.1111/j.1365-3091.1974.tb02067.x

Gostick, J. T. (2017). Versatile and efficient pore network extraction method using marker-based watershed segmentation. *Physical Review E*, *96*(2). https://doi.org/10.1103/PhysRevE.96.023307

Gostick, J. T., Aghighi, M., Hinebaugh, J., Tranter, T., Hoeh, M. A., Day, H., … Putz, A. (2016). OpenPNM: A Pore Network Modeling Package. *Computing in Science & Engineering*, *18*(4), 60–74. https://doi.org/10.1109/MCSE.2016.49

Hartfield, G., Blunden, J., Arndt, D. S., Hartfield, G., Blunden, J., & Arndt, D. S. (2018). State of the Climate in 2017. *Bulletin of the American Meteorological Society*, *99*(8), Si-S310. https://doi.org/10.1175/2018BAMSStateoftheClimate.1

Hollis, C., Bastesen, E., Boyce, A., Corlett, H., Gawthorpe, R., Hirani, J., … Whitaker, F. (2017). Fault-controlled dolomitization in a rift basin. *Geology*, *45*(3), 219–222. https://doi.org/10.1130/G38s394.1

Kärger, J. (2011). Flow and Transport in Porous Media and Fractured Rock. *Zeitschrift Für Physikalische Chemie*, *194*(Part_1), 135–136. https://doi.org/10.1524/zpch.1996.194.part_1.135a

Krevor, S., Blunt, M. J., Benson, S. M., Pentland, C., Reynolds, C., Al-Menhali, A., & Niu, B. (2015). Capillary trapping for geologic carbon dioxide storage – From pore scale physics to field scale implications. *International Journal of Greenhouse Gas Control*, *40*, 221–237. https://doi.org/10.1016/J.IJGGC.2015.04.006

Kuijpers, C. J., Huinink, H. P., Tomozeiu, N., Erich, S. J. F., & Adan, O. C. G. (2017). Sorption of water-glycerol mixtures in porous Al2O3 studied with NMR imaging. *Chemical Engineering Science*, *173*, 218–229. https://doi.org/10.1016/J.CES.2017.07.035

Marone, F., & Stampanoni, M. (2012). Regridding reconstruction algorithm for real-time tomographic imaging. *Journal of Synchrotron Radiation*, *19*(Pt 6), 1029–1037. https://doi.org/10.1107/S0909049512032864

Mason, G., & Morrow, N. R. (1991). Capillary behavior of a perfectly wetting liquid in irregular triangular tubes. *Journal of Colloid and Interface Science*, *141*(1), 262–274. https://doi.org/10.1016/0021-9797(91)90321-X

Otsu, N. (1979). A Threshold Selection Method from Gray-Level Histograms. *IEEE Transactions on Systems, Man, and Cybernetics*, *9*(1), 62–66. https://doi.org/10.1109/TSMC.1979.4310076

Patzek, T. W. (2001). Verification of a Complete Pore Network Simulator of Drainage and Imbibition. *SPE Journal*, *6*(02), 144–156. https://doi.org/10.2118/71310-PA

Patzek, T. W., & Kristensen, J. G. (2001). Shape Factor Correlations of Hydraulic Conductance in Noncircular Capillaries: II. Two-Phase Creeping Flow. *Journal of Colloid and Interface Science*, *236*(2), 305–317. https://doi.org/10.1006/JCIS.2000.7414

Qin, C.-Z. (2015). Water Transport in the Gas Diffusion Layer of a Polymer Electrolyte Fuel Cell: Dynamic Pore-Network Modeling. *Journal of The Electrochemical Society*, *162*(9), F1036–F1046. https://doi.org/10.1149/2.0861509jes

Qin, C.-Z., Hassanizadeh, S. M., & Van Oosterhout, L. M. (2016). Pore-Network Modeling of Water and Vapor Transport in the Micro Porous Layer and Gas Diffusion Layer of a Polymer Electrolyte Fuel Cell. *Computation*, *4*(2), 21. https://doi.org/10.3390/computation4020021

Randolph, J. B., & Saar, M. O. (2011). Combining geothermal energy capture with geologic carbon dioxide sequestration. *Geophysical Research Letters*, *38*(10), n/a-n/a. https://doi.org/10.1029/2011GL047265

Rasmusson, K., Rasmusson, M., Tsang, Y., & Niemi, A. (2016). A simulation study of the effect of trapping model, geological heterogeneity and injection strategies on CO2 trapping. *International Journal of Greenhouse Gas Control*, *52*, 52–72. https://doi.org/10.1016/J.IJGGC.2016.06.020

Rasmusson, M. (2018). *Residual and Solubility trapping during Geological CO2 storage : Numerical and Experimental studies*. *Digital Comprehensive Summaries of Uppsala Dissertations from the Faculty of Science and Technology NV - 1640*. Acta Universitatis Upsaliensis, LUVAL, Department of Earth Sciences, Earth Sciences, Disciplinary Domain of Science and Technology, Uppsala University.

Retrieved from http://uu.diva-portal.org/smash/get/diva2:1187364/FULLTEXT01.pdf

Soille, P. (2014). Morphological Image Analysis: Principles and Applications. *Sensor Review*, *20*(3), 391. https://doi.org/10.1108/sr.2000.08720cae.001

Valvatne, P. H., & Blunt, M. J. (2004). Predictive pore-scale modeling of two-phase flow in mixed wet media. *Water Resources Research*, *40*(7). https://doi.org/10.1029/2003WR002627

APPENDIX A

Relations of capillary pressure and phase conductivities for idealized pore elements

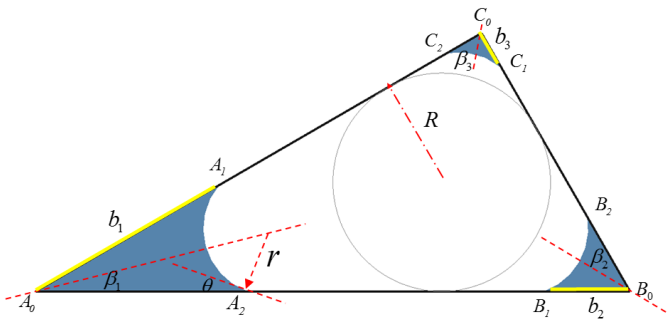

Fig A1: Wetting phase (in blue) distributions in a pore element, which has a triangular cross section. The three half corner angles, β_1, β_2, and β_3, are 15°, 30°, and 45° respectively. θ is the static contact angle, R is the radius of the inscribed circle, r is the radius of the nonwetting-wetting interface curvature, and b denotes the distance from each apex to the corresponding nonwetting-wetting interface along the solid wall (in yellow).

Capillary pressure

The capillary entry pressure for a pore body or a pore throat is calculated by the following nonlinear equations based on the MS-P theory (Patzek, 2001):

$$r = \frac{A_{eff}}{L_{nw} + L_{ns}\cos\theta} \tag{6}$$

$$A_{eff} = A - R^2 \sum_{i=1}^{n} \left[\frac{\cos\theta\cos(\theta+\beta_i)}{\sin\beta_i} + \theta + \beta_i - \frac{\pi}{2} \right] \tag{7}$$

$$L_{ns} = \frac{R}{2G} - 2\sum_{i=1}^{n} b_i \tag{8}$$

$$L_{nw} = 2r\sum_{i=1}^{n} asin\left(\frac{b_i \sin\beta_i}{r} \right) \tag{9}$$

$$b_i = r\frac{\max(0, \cos(\theta+\beta_i))}{\sin\beta_i} \tag{10}$$

where A_{eff} is the cross-sectional area for the nonwetting phase, A is the cross-sectional area of the pore body, L_{nw} and L_{nw} denote the length of nonwetting-wetting interface and the length of the nonwetting-wall interface, respectively, and for the remaining notations, one can refer to Fig. A1.

For a pore body with the cross section of the right triangle described in Fig. A1, assuming $R = 20\mu m$ and the surface tension of 0.073 N/m, the obtained entry capillary pressure versus the static contact angle is plotted in Fig. A2a. Also, the corresponding distances, b_1, b_2, and b_3 are plotted. The distances go to zero if corner flow cannot be formed.

For the piston-type move of AMs, taking the parameters used in Fig. A2a, the capillary pressure versus saturation curves are plotted in Fig. A2b for four contact angle values. Notice that each curve is truncated at its snap-off saturation. The snap-off event is triggered once more than one AM touch each other. For a triangle cross-section, we check the following three inequalities:

$$b_1 + b_3 < l_{A_0C_0} \tag{11}$$

$$b_1 + b_2 < l_{A_0B_0} \tag{12}$$

$$b_2 + b_3 < l_{B_0C_0} \tag{13}$$

where l denotes the side length. If one or more are false, the snap-off is triggered. When the snap-off occurs, the nonwetting phase is trapped in the pore body.

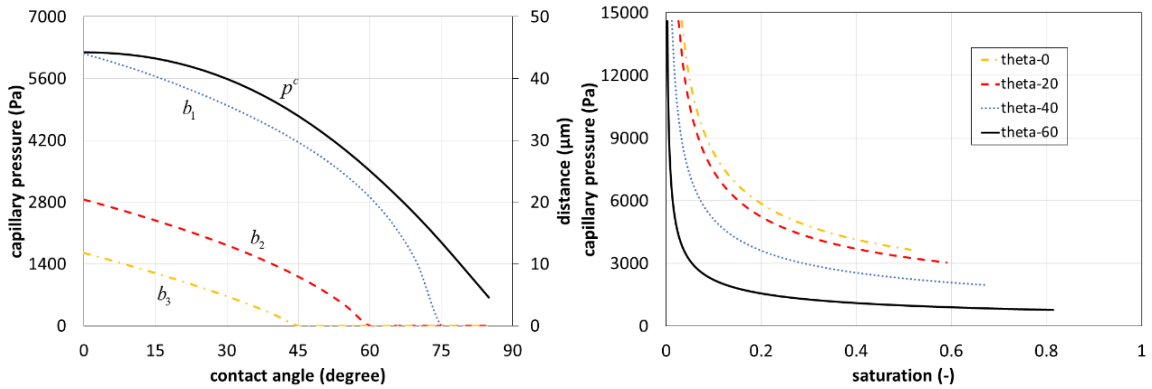

Fig. A2: (a) imbibition entry capillary pressure versus the static contact angle, and the corresponding distances, b_1, b_2, and b_3; (b) the capillary pressure versus the wetting saturation at four different contact angle values. The cross section is the right triangle, the inscribed circle radius is 20 μm, and the surface tension is 0.073 N/m.

Phase conductance

Flow resistance in both pore bodies and pore throats is taken into account. If a pore is fully filled by either nonwetting or wetting phase, the single-phase conductance is given by (Patzek & Kristensen, 2001):

$$g = \begin{cases} 0.6GS^2 & triangle \\ 0.5632GS^2 & square \\ 0.5GS^2 & circle \end{cases} \tag{14}$$

where g is the conductance.

If a pore is occupied by both nonwetting and wetting phases, the conductance for the wetting phase is calculated as follows. First, for an AM (see Fig. A1), with $b=1$, the dimensionless corner wetting area is given as (Patzek & Kristensen, 2001):

$$\tilde{A}^w = \left(\frac{\sin\beta}{\cos(\theta+\beta)}\right)^2 \left(\frac{\cos\theta\cos(\theta+\beta)}{\sin\beta} + \theta + \beta - \frac{\pi}{2}\right) \tag{15}$$

Further, we define the shape factor for the corner wetting as:

$$\tilde{G}^w = \frac{\tilde{A}^w}{4\left[1-(\theta+\beta-\pi/2)\sin\beta/\cos(\theta+\beta)\right]} \tag{16}$$

Then, the semi-empirical dimensionless conductance with the perfect slip boundary condition between wetting and nonwetting phases is calculated by (Patzek & Kristensen, 2001):

$$\tilde{g}^w = \exp\left\{\left[-18.2066\left(\tilde{G}^w\right)^2 + 5.88287\tilde{G}^w - 0.351809 + 0.02\sin\left(\beta-\pi/6\right)\right] \Big/ \left(1/4/\pi - \tilde{G}^w\right) + 2\ln S^w\right\} \tag{17}$$

Finally, the dimensional one is obtained as $g^w = \left(b^4/\mu\right)\tilde{g}^w$. Taking the parameters used in Fig. A3, Fig. A4 shows the curves of conductance versus saturation for four contact angle values. Obviously, for the same saturation value, a larger contact angle gives larger wetting-phase conductance along the corners. For the nonwetting-phase conductance, it is approximated by (Qin, 2015):

$$g^n = \begin{cases} 0.6GS\left(1-A^w\right) & triangle \\ 0.5632GS\left(1-A^w\right) & square \end{cases} \tag{18}$$